Quantum Electronics **48** (3) 189–196 (2018)

INVITED PAPER

https://doi.org/10.1070/QEL16574

Spectral characterisation of aperiodic normal-incidence Sb/B_4C multilayer mirrors for the $\lambda < 124$ Å range

E.A. Vishnyakov, I.A. Kopylets, V.V. Kondratenko, A.O. Kolesnikov, A.S. Pirozhkov, E.N. Ragozin, A.N. Shatokhin

Abstract. **Three broadband aperiodic Sb/B_4C multilayer mirrors were synthesised for the purposes of soft X-ray optics and spectroscopy in the wavelength range beyond the L-edge of Si ($\lambda < 124$ Å), and their reflection spectra were measured. The multilayer structures were optimised for maximum uniform reflectivity in the ranges 100–120 Å, 95–105 Å and 90–100 Å. The reflection spectra were recorded using a laboratory laser-plasma radiation source and an electronic detector with a 2D spatial resolution (a CCD matrix with 13 × 13 μm sized pixels). The experimental spectra are compared with theoretical calculations. The effect of lower antimony and B_4C layer densities on the reflection spectra is discussed.**

Keywords: *soft X-ray range, multilayer mirrors, antimony, boron carbide, Sb/B_4C, aperiodic structures, normal radiation incidence.*

1. Introduction

Modern reflective normal-incidence X-ray multilayer optics is an important tool of basic and applied physics research in soft X-ray (SXR) and vacuum ultraviolet (VUV) spectral regions ($\lambda = 10–1000$ Å) [1–4]. Multilayer mirrors (MMs) enjoy wide use in telescopic, spectral and polarimetric instruments for the diagnostics of plasmas (both laboratory [5–8] and astrophysical [9–12]), in devices intended for the detection and analysis of SXR radiation produced by high-brightness beam accelerators (including synchrotrons [13] and free-electron lasers [14]), in the new instrumentation intended for X-ray photolithography [2, 3], etc.

As before, the easiest to manufacture are periodic MMs, which are, in the simplest case, bilayer structures M times reproduced on a prefabricated substrate of requisite shape. Such MMs exhibit highly selective reflection spectra, which permits using them for the extraction of specific lines or line arrays from line spectra. The most frequently used characteristic of periodic MMs is the peak reflectivity (i.e. the reflectivity at a wavelength $\lambda_0 = 2d\langle n\rangle\cos\theta$, where d is the period of the multilayer structure, $\langle n\rangle$ is the period-averaged refractive index, and θ is the angle of radiation incidence.

At the same time there appears an increasing number of problems whose solution calls for a greater diversity of the spectral reflectivity MM profiles to meet more sophisticated functional requirements. These are, for instance, the simultaneous maximisation of reflectivities at two or more given wavelengths [15], the attainment of a high reflectivity at a specific wavelength throughout a broad range of incidence angles [16] or the attainment of the highest possible uniform reflectivity in a given spectral range [17]. These problems are successfully solved with the use of aperiodic multilayer mirrors (AMMs), for which the notion of period is most often nonexistent in principle, each layer having its own individual thickness d_i.

The AMM layer thickness distribution is usually calculated with numerical techniques to solve the inverse problem of multilayer optics by minimising some functional, which defines the measure of the difference between the AMM spectral reflectivity $R(\theta,\lambda)$ and the target spectral reflectivity F_{gf} [18]. Sometimes introduced in the minimised functional are additional conditions, for instance, for the purpose of lowering the variation of the thicknesses of closely located layers of each of the materials to improve the stoichiometric layer uniformity throughout the structure [19]. The spectral AMM reflectivity function calculated at each iteration is determined by the method of recurrence relations [20, 21], which has repeatedly been employed by many researchers.

Nowadays the technology of fabricating Mo/Si multilayers has been well mastered, which permits synthesising structures of different types for various applications. In particular, Mo/Si AMMs designed by the method of Ref. [18] were employed to record the spectra in several experiments aimed at investigating elementary processes with participation of multiply charged ions [5–7], for the diagnostics of laboratory laser plasmas [22–24], in experiments on the conversion of the frequency of a multiterawatt Ti:sapphire laser ($\lambda \sim 0.8$ μm) in the reflection from a relativistic plasma wave driven by the laser in a pulsed He jet (the relativistic 'flying mirror') [25, 26]. As shown in Refs [27, 28], Mo/Si AMMs with controlled phase of reflected SXR spectral components are applicable for reflecting attosecond SXR radiation pulses and converting their duration, which was more recently demonstrated in several experimental papers, for instance in Ref. [29]. The experiments which make use of Mo/Si AMMs are more amply discussed in review Refs [30, 31].

E.A. Vishnyakov, E.N. Ragozin P.N. Lebedev Physical Institute, Russian Academy of Sciences, Leninsky prosp. 53, 119991 Moscow, Russia; e-mail: juk301@mail.ru; enragozin@gmail.com;
I.A. Kopylets, V.V. Kondratenko National Technical University 'Kharkiv Polytechnic Institute', ul. Kirpicheva 21, 61002 Kharkiv, Ukraine;
A.O. Kolesnikov, A.N. Shatokhin P.N. Lebedev Physical Institute, Russian Academy of Sciences, Leninsky prosp. 53, 119991 Moscow, Russia; Moscow Institute of Physics and Technology (State University), Institutskii per. 9, 141701 Dolgoprudnyi, Moscow region, Russia;
A.S. Pirozhkov Kansai Photon Science Institute, National Institutes for Radiological Science and Technology, 8-1-7 Umemidai, Kizugawa-city, Kyoto, 619-0215, Japan

Received 14 November 2017; revision received 9 January 2018
Kvantovaya Elektronika **48** (3) 189–196 (2018)
Translated by E.N. Ragozin

However, Mo/Si MMs may be validly used only in the range $\lambda > 124$ Å (down to the L edge of Si) because of the high absorption of shorter-wavelength SXR radiation in silicon layers. This circumstance has long spurred the quest for promising material pairs for the synthesis of MMs in the $\lambda < 124$ Å range. Artyukov et al. [32] analysed the optical properties of more than 1300 inorganic compounds and elements, and selected material pairs as components for periodic MMs for wavelengths of 30–300 Å. Late in the XXth century, Mo/Be and Mo/Y MMs showed the greatest promise in the spectral range bounded above by the L absorption edge of Si ($\lambda = 124$ Å) and bounded below by the K absorption edge of boron ($\lambda = 65.9$ Å). For example, Skulina et al. [33] reported the synthesis of periodic Mo/Be and Nb/Be MMs, which exhibited peak reflectivities $R = 69\%$ and 58%, respectively, at a wavelength $\lambda = 113$ Å. More recently, however, in a shorter-wavelength region it was possible to attain reflectivities of 34% at $\lambda = 95.0$ and 93.4 Å in periodic Mo/Y [34] and Ru/Y [3] MMs, respectively. Work on La/B_4C structures resulted in the synthesis of a periodic La/B_4C/C MM with a carbon barrier layer, which exhibited a remarkable reflection coefficient of 58.6% at $\lambda \approx 67$ Å for an incidence angle of 20° [35].

In Ref. [30], the optical constants of 18 materials devoid of absorption edges in the 80–125 Å range were analysed from the standpoint of fabrication of AMMs in the 80–130 Å range. Pd/Y, Pd/B_4C, and Ag/Y material pairs were shown to hold good promise. Corso et al. [36] synthesised Pd/B_4C MMs with peak reflectivities of 42% at $\lambda = 66.7$ Å (at an incidence angle $\varphi = 45°$) and 43% at $\lambda = 91$ Å at near-normal incidence of radiation. However, it turned out that Pd/B_4C structures possessed a high internal stress of about 1200 MPa. Recent experimental investigations showed that the best results in the 80–120 Å spectral range are exhibited by Pd/Y structures with B_4C barrier layers ($R = 43\%$ at $\lambda = 93$ Å for periodic MMs and a relatively uniform reflectivity $R \approx 5\%$ for AMMs in the 88–113 Å range [37].

The present work is concerned with experimental and theoretical investigations of Sb/B_4C AMMs for the 90–120 Å range. Attention to this structure was first drawn in Ref. [38]. Several periodic Sb/B_4C MMs were earlier synthesised for a $\lambda < 125$ Å range, and their peak reflectivities at $\lambda = 84.3$ and 85.5 Å were measured at 18.0% and 19.6%, and those at $\lambda = 67.7$ and 66.3 Å were measured at 19.9% and 28.5%, respectively [39, 40]. According to estimates, transition layers in Sb/B_4C structures are thin (below 10 Å) and the stability of the synthesised mirrors turns out to be very high (in a year of storage in the air the relative MM reflectivities lowered by no more than 3%), which furnishes the possibility to make stable broadband Sb/B_4C AMMs for spectroscopic applications.

Below we discuss the experimentally recorded reflection spectra of Sb/B_4C AMMs optimised for maximum uniform reflectivity in the ranges 100–120 Å, 95–105 Å, and 90–100 Å. In the future, we plan to use these AMMs in high-resolution VLS spectrometers which combine the advantages of broadband normal-incidence X-ray MMs and varied line-space reflection gratings [41–43]. The AMMs under investigation were synthesised at the NTU 'Kharkov Polytechnic Institute' and then tested in the LPI using a scheme with a laser-plasma SXR source. The experimentally recorded spectra are analysed and compared with the spectra calculated by numerical simulations.

2. Fabrication of the mirrors and experimental facility

The broadband Sb/B_4C AMMs under study were synthesised by magnetron sputtering on polished spherical substrates of fused silica 40.0 mm in diameter. The magnetron targets of Sb and B_4C were sputtered in the atmosphere of argon at a pressure of 1.8×10^{-3} Torr. The concave fused silica substrates for the AMMs had a radius of curvature of 1000 mm and a surface roughness $\sigma \approx 3.5$ Å. As indicated by earlier investigations, the first layer to be deposited on the substrate is a B_4C layer to provide a high stability of the Sb/B_4C structure: otherwise, the mirror exfoliates within a year [39]. Consequently, boron carbide makes up the first and last structure layers in all of the AMMs discussed in our work.

The magnetrons were fed by stabilised power supplies to provide a constant target sputtering rate. The deposited layer thicknesses were controlled by the time of substrate residence above the magnetron, which was controlled by an automatic substrate displacement system with an accuracy of 1 ms.

Prior to AMM fabrication, preliminary experiments were performed to determine the Sb and B_4C layer deposition rates. To this end, a series of periodic MMs were made for the same deposition conditions and with different Sb and B_4C layer deposition times. The period of each of the periodic MMs was determined from the measured angular positions of the Bragg peaks in low-angle X-ray reflectograms recorded at $\lambda = 1.54$ Å (the K_α line of copper, Cu-K_α in what follows) with the use of the Bragg–Wolf equation and the values of refractive indices. The Sb and B_4C deposition rates were obtained by dividing the difference between the periods of the pair of periodic MMs by the difference in the deposition times for the corresponding material layers. The antimony and B_4C layer growth rates were equal to 1.977 and 2.344 Å s^{-1}, respectively.

To verify the correspondence between the synthesised Sb/B_4C structures and the calculated AMMs, a so-called witness mirror was deposited on a plane glass substrate in each working AMM deposition process. Both mirrors were simultaneously coated in one deposition run (Fig. 1a), the substrates being attached to the opposite ends of the rotating carousel. Under this geometry, a B_4C layer is deposited on the witness mirror when an Sb layer is deposited on the AMM, and vice versa. After the deposition of each layer on the AMM, the carousel is rotated by 180° about the axis. The *i*th layer deposition time is the same for both mirrors and is borrowed from numerical simulations, but the oppositely mounted substrates are always coated with different materials. Therefore, the multilayer structure of the witness mirror 'complements', in a sense, the synthesised AMM structure.

After deposition, low-angle X-ray reflectograms of the witness mirrors were recorded with Cu-K_α radiation in a θ–2θ scanning geometry using a DRON-3M diffractometer, which operated in a two-crystal scheme with a silicon crystal monochromator placed in the primary beam. The primary beam divergence was equal to 0.015°. The measured reflectograms of the witness mirrors were compared with the data of numerical simulations (this comparison is exemplified in Fig. 1b). One can see that the experimental and simulation curves agree nicely. This is indication that the AMM layer thicknesses are also close to the requisite ones.

Figure 2 is a schematic representation of the imaging (stigmatic) diffraction spectrometer employed for measuring the reflection spectra of Sb/B_4C AMMs. The spectrometer, which

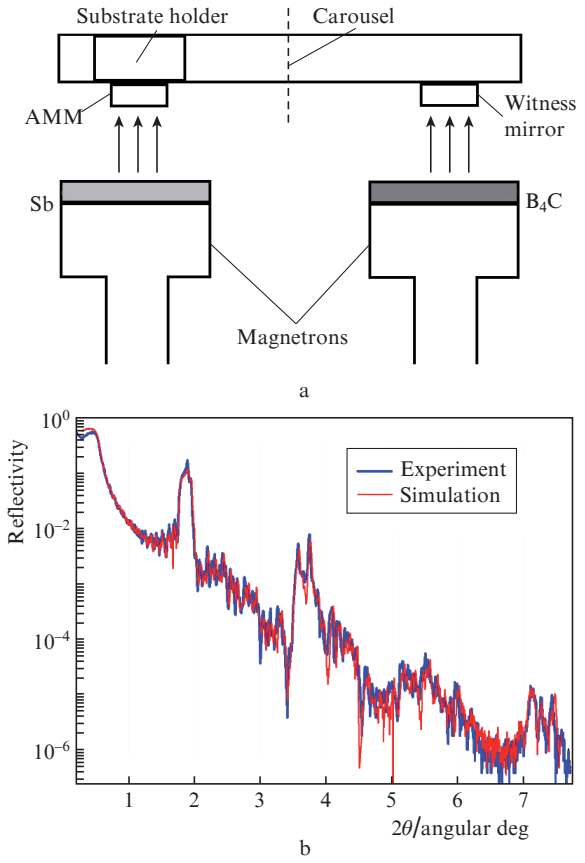

Figure 1. Schematic of the AMM deposition facility with a witness mirror at the opposite end of the carousel (a) as well as measured and calculated reflectograms (θ–2θ, Cu-K_α, λ = 1.54 Å) of the witness mirror for the AMM optimized for the 90–100 Å range (b).

is similar to that used in Ref. [44], was assembled on an optical table of size 0.6 × 3.6 m, which was placed in the 3.8-m long 'Ikar' vacuum chamber 0.9 m in diameter equipped with an oil-free pump. The spectrometer comprised a 60-μm wide entrance slit, an AMM under study, a transmission diffraction grating (DG), and a detector.

The SXR source was the laser plasma produced by focusing nanosecond laser pulses (Nd:YAG laser, E = 0.5 J, τ = 8 ns, λ = 1.064 μm) onto a tungsten target with a heavy flint lens with focal length f = 75 mm. The laser beam was focused to a spot with an effective area $S_{\text{eff}} \approx 10^{-5}$ cm^2. In this case, the peak intensity of laser radiation at the focal spot centre amounted to $\sim 10^{13}$ W cm^{-2}. Under these intensities, the resultant tungsten plasma radiation was a quasi-continuous spectrum with a smoothly varying intensity in a broad wavelength range (20–250 Å) [45, 46]. This permits using the emission of this source for characterising broadband SXR AMMs. Reflection spectra were recorded in one laser shot; also used were series of three to five shots.

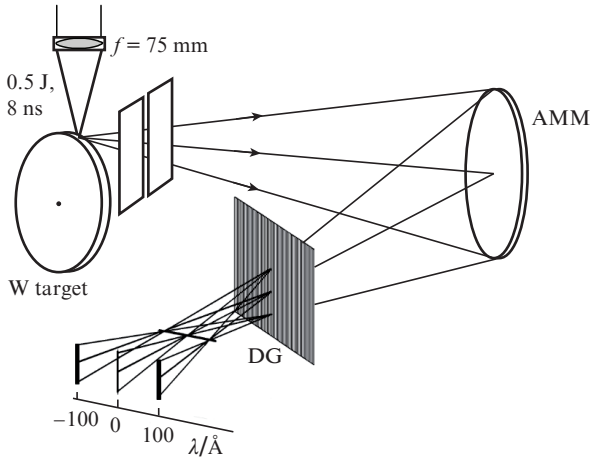

Figure 2. Schematic diagram of the SXR diffraction spectrometer.

The function of the dispersing element of the spectrometer was fulfilled by a free-standing DG with a line density of 1000 mm^{-1} and an aperture of size 20 × 20 mm, which was placed in the beam reflected from the AMM under study. The resultant spectra were recorded with an uncooled backside-illuminated CCD 47-10 matrix with a dynamic range of ~100, a pixel size of 13 × 13 μm, and a working area of 1024 × 2048 pixels, whose sensitivity was measured in a broad spectral range in Refs [8, 47]. The recorded spectra are the product of the emission spectrum of the tungsten plasma, the spectral reflectivity of the AMM, and the spectral responsivity of the CCD detector.

The entrance slit of the spectrometer and the CCD matrix were located on the Rowland circle of the AMM under study and were placed symmetrically relative to normal to the mirror surface drawn through the point of incidence of the central ray. The distance between the entrance slit and the middle of the CCD was equal to 150 mm, thereby making small the angles of radiation incidence on and reflection from the MM (0.07 ± 0.01 rad). Such near-normal-incidence configurations possess small aberrations, with the result that the spectral images of the slit produced by the mirrors under study on the sensitive detector surface were highly stigmatic. In the measurements the plate scale was equal to 24 Å mm^{-1} and the spectral slit width was equal to 1.5 Å.

The SXR source (the tungsten laser plasma) was located outside of the AMM Rowland circle at a distance of ~100 mm from the entrance slit. This mutual arrangement of the entrance slit and the source makes the measuring scheme somewhat astigmatic (Fig. 2), which may be used to characterise the coating uniformity over the AMM aperture. Each horizontal pixel line contains a portion of the spectrum with information about the radiation reflected from a relatively small segment of the MM surface ~1 mm in height. In particular, small fluctuations of AMM layer thicknesses in different vertical portions of the aperture may have a rather strong effect on the AMM reflection spectrum, which would be revealed by the spectral images recorded by the CCD detector.

3. Experimental results and their discussion

In this work an experimental study was made of three normal-incidence Sb/B_4C AMMs. The structures were designed for maximum uniform reflectivity in different spectral intervals within the wavelength range 90–120 Å (Table 1) and then deposited on concave fused silica substrates. The Sb/B_4C AMMs under study contained 150 layers each (75 layer pairs).

Figure 3 gives examples of the experimentally recorded reflection spectrum of the AMM optimised for the 95–105 Å range and the digitised spectra of the three AMMs. One can see diffraction orders m = 0, 1, and -1. Furthermore, one can clearly see regular peaks in the spectrum about the zero dif-

Table 1. Parameters of the Sb/B_4C AMMs under investigation.

Optimisation range/Å	Number of layers $2M$ in the AMM	Average volume fraction of B_4C in the MM	Target optimisation parameter R_0 (%)	Real working spectral domain/Å
90–100	150	0.53	6.03	90.5–100.0
95–105	150	0.55	7.51	96.5–105.5
100–120	150	0.59	5.02	101.5–121.5

fraction order (on either side of it). These peaks are produced due to diffraction of exciting laser radiation (λ = 1.064 μm) by the grating support structure (the period of DG support structure is equal to 1.25 mm). The exciting laser radiation may find its way into the spectrometer on reflection from the laser plasma or from the tungsten target, which is slightly inclined to the spectrometer axis (Fig.2).

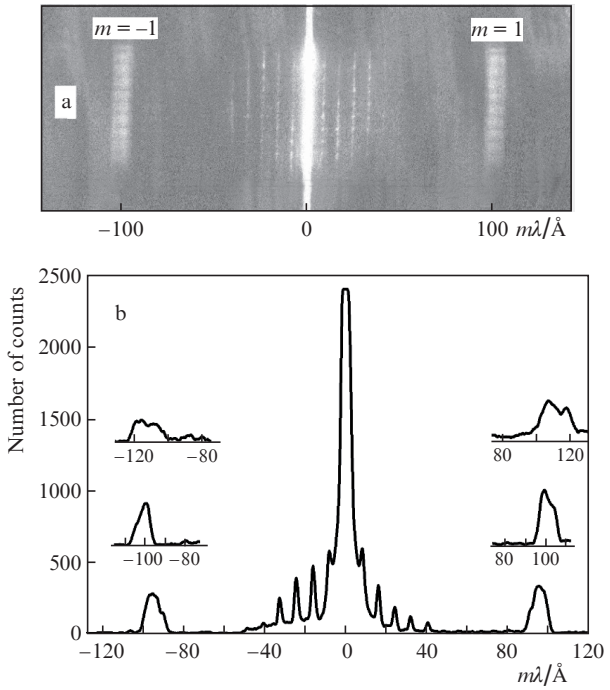

Figure 3. Experimentally recorded reflection spectrum of the AMM optimised for the 95–105 Å range (a) and digitised spectra of all three Sb/B_4C AMMs under investigation (b).

The spectra in the working diffraction orders $m = \pm 1$ in Fig. 3a are uniform vertical bands of nearly constant width, which are additionally modulated by the grating support structure. The constant width of these bands testifies to a high uniformity of the multilayer coating throughout the AMM aperture (the edges of the working spectral region in the aperture of each AMM retain their position to within ~0.5 Å).

Figures 4a, 4c and 4e depict the experimentally recorded and simulation reflection spectra of the three Sb/B_4C AMMs. Plotted in Figs 4b, 4d and 4f are the antimony and boron carbide layer thickness distributions in the synthesised aperiodic multilayer structures (the layer number increases towards the substrate). In the simulations, the admissible layer thickness was bounded below by 15 Å. This makes the AMMs suitable from the synthesis standpoint, because the deposition of thinner layers is technically difficult. As the AMM optimisation range shifts to the longer-wavelength side, the volume-averaged B_4C fraction in the multilayer structures increases from 0.53 to 0.59 (Table 1). In periodic Sb/B_4C MMs the optimal volume B_4C fraction is equal to 0.53 [39].

One can see in Fig. 4 that the working spectral domains of all synthesised mirrors are shifted to the long-wavelength side relative to the optimisation ranges (see also Table 1). This may be attributed to the departure of real AMM layer material densities from the tabulated ones.

The optical and spectral AMM properties are defined by the layer thicknesses of the binary structure $(A/B)_M$ and the complex material permittivities $\varepsilon_{A,B} = n^2_{A,B} = 1 - \delta_{A,B} + i\beta_{A,B}$. For materials consisting of different atoms (for instance, B_4C), the optical constants δ and β may be defined in terms of the atomic scattering factors $f = f_1 + if_2$ of the atoms of these sorts. Let α_i be the fraction of atoms of sort i in the material involved. Then, according to Ref. [48],

$$\begin{pmatrix}\delta\\ \beta\end{pmatrix} = \frac{r_0}{\pi}\lambda^2\begin{pmatrix}\sum\limits_i N_i f_{1i}\\ \sum\limits_i N_i f_{2i}\end{pmatrix} \approx 0.54\times 10^{-5}\frac{\rho}{\sum\limits_i \alpha_i\mu_i}\tilde{\lambda}^2\begin{pmatrix}\sum\limits_i \alpha_i f_{1i}\\ \sum\limits_i \alpha_i f_{2i}\end{pmatrix},$$

where $r_0 = e^2/(m_e c^2) \approx 2.8 \times 10^{-13}$ cm is the classical electron radius; N_i is the density of atoms of sort i; the wavelength $\tilde{\lambda}$ is expressed in Angström units; ρ is the density of the compound material in grams per cubic centimetre; and μ_i is the weight of atoms of sort i in atomic mass units.

The direct problem of multilayer optics (determination of the spectral reflectivity of a multilayer structure with known optical material constants) has been traditionally solved by the method of recurrence relations [20, 21]. This problem has to be solved at each iteration of the optimisation problem (the inverse problem), in which, however, the material densities are defined by the user and are not optimised. The initial calculated spectral dependences of the reflection coefficients of the three synthesised Sb/B_4C AMMs discussed in the present work were found under the assumption that the Sb and B_4C layer densities coincide with the tabulated ones. All AMMs were calculated by minimising the functional [18]

$$\Im_1 = \int [R(\lambda) - R_0]^2 \mathrm{d}\lambda,$$

where R_0 is the target optimisation parameter (see Table 1) and $R(\lambda)$ is the calculated spectral reflectivity dependence of the Sb/B_4C AMM obtained by the method of recurrence relations. The integration was performed over the AMM optimisation domain.

In the initial calculations the AMM material layer densities were assumed to be equal to the tabulated bulk material densities ρ(Sb) = 6.7 g cm^{-3} and $\rho(B_4C)$ = 2.5 g cm^{-3}, and the atomic scattering factors were borrowed from the tables of Ref. [48]. However, after the investigation of periodic Sb/B_4C MMs and a careful analysis of the resultant data [39, 40] it became clear that the layer densities do not correspond to the

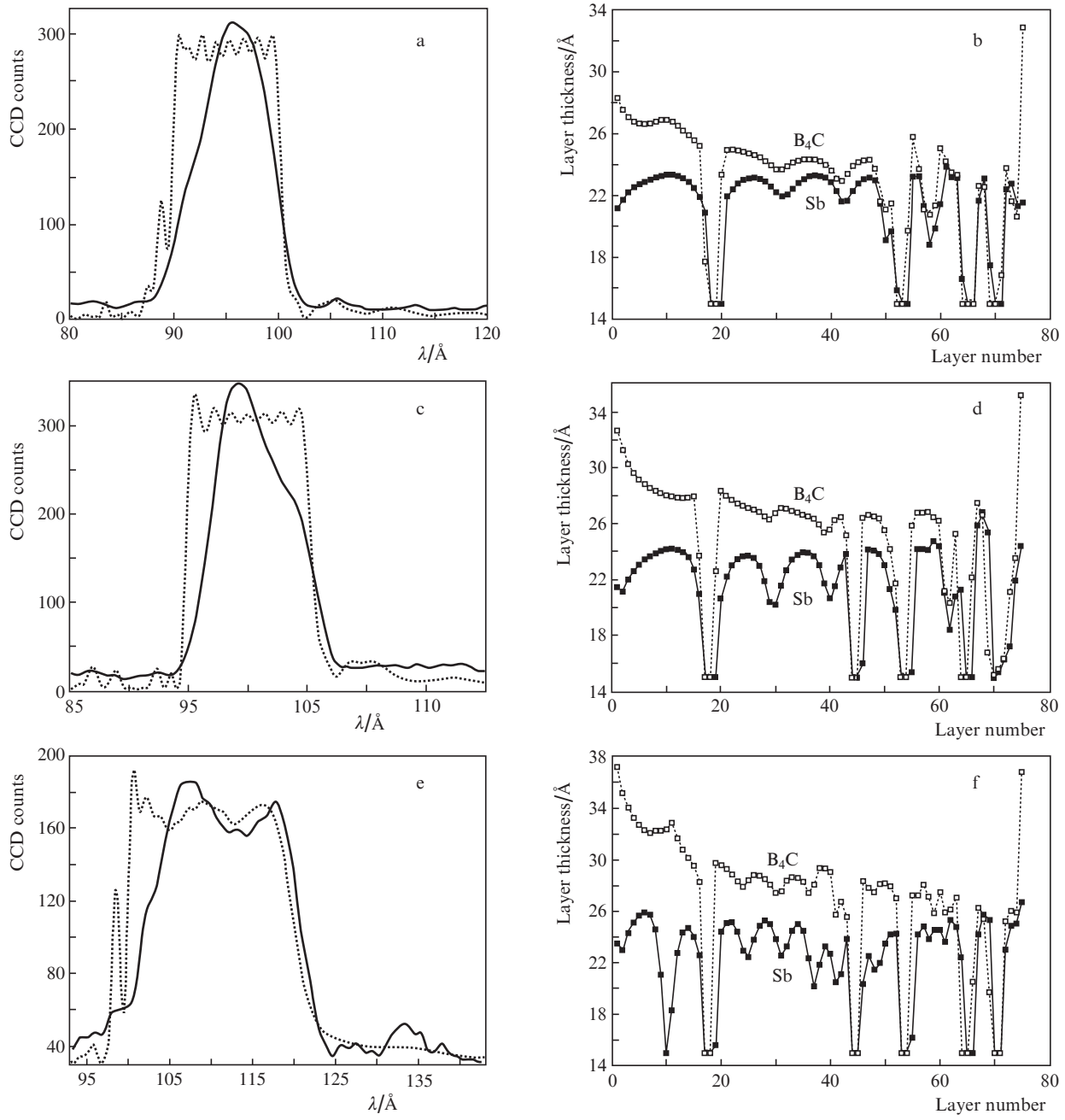

Figure 4. Reflection spectra (a, c, e) and layer thicknesses of the multilayer structures (b, d, f) of Sb/B_4C AMMs optimised for the spectral ranges 90–100 Å (a, b), 95–105 Å (c, d), and 100–120 Å (e, f). The solid curves in the spectra (a, c, e) correspond to experimental data and the dotted lines correspond to numerical simulations reliant on the tabulated material densities. Each structure contains 150 layers.

tabulated values. After this, corrections had to be introduced into our calculations.

Figure 5 shows how the Sb and B_4C layer density variation affects the reflection spectrum of the AMM optimised for maximum uniform reflectivity in the 95–105 Å range. Initial curve (*1*) was obtained assuming the tabulated bulk material densities $\rho(Sb) = 6.7$ g cm^{-3} and $\rho(B_4C) = 2.5$ g cm^{-3}. In the calculation of spectral curve (*2*) the antimony density $\rho(Sb) = 6.0$ g cm^{-3} was borrowed from Ref. [39]. One can see that the average AMM reflection coefficient lowers from 7.5% to 5.5% on lowering the antimony layer density by 10%, from 6.7 to 6.0 g cm^{-3}. An even lower value, $\rho(Sb) = 5.3$ g cm^{-3}, was obtained from low-angle X-ray scattering of the Cu-K_α line ($\lambda = 1.54$ Å) in Ref. [40]. The calculation assuming this antimony layer density [curve (*3*) in Fig. 6] gives an even greater decrease of the average AMM reflection coefficient down to 3.5%. However, when it is considered that the density of thin B_4C layers may also be lower than the tabulated value in certain cases (in La/B_4C MMs the density $\rho(B_4C) = 1.8$ g cm^{-3} [35]), the optical contrast between the layers of antimony and boron carbide may rise again, which will entail an increase of the average AMM reflection coefficient to 6% [spectral curve (*4*) in Fig. 5]. The antimony and boron carbide densities employed in the numerical calculations of the AMM reflection spectra in Fig. 5 are collected in Table 2.

Worthy of mention is another feature of the simulation spectra in Fig. 5. Each lowering of the layer density of one of the AMM materials results in a small shift of the AMM work-

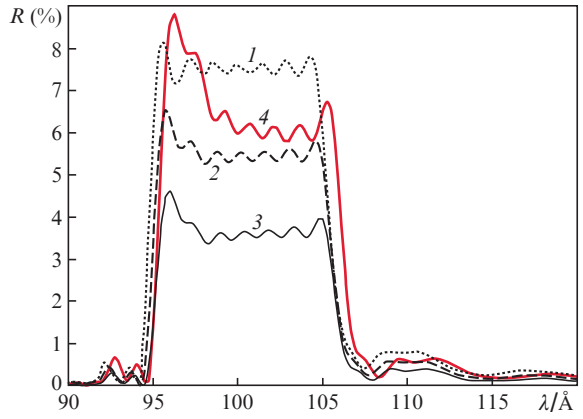

Figure 5. Calculated reflection spectra of the Sb/B_4C AMM optimised for the 95–105 Å range, which were obtained for ρ(Sb) = 6.7 (*1*), 6.0 (*2*), and 5.3 g cm^{-3} (*3*, *4*), as well as for $\rho(B_4C)$ = 2.5 (*1*–*3*) and 1.8 g cm^{-3} (*4*). All layer thicknesses in the structures under comparison are the same.

Table 2. Sb and B_4C layer densities employed in the simulation of reflection spectra of the AMM optimised for the 95–105 Å range (Fig. 5).

Spectrum number	ρ(Sb)/g cm^{-3}	$\rho(B_4C)$/g cm^{-3}
1 (initial)	6.7	2.5
2	6.0	2.5
3	5.3	2.5
4	5.3	1.8

ing spectral domain towards longer wavelength, which was also seen in experiment (see Fig. 4, Table 1). The shift of the working spectral domains of all AMMs under study relative to the initial simulations is attributable to the increase in structure-averaged refractive index $\langle n \rangle$ due to the lowering of layer material densities.

As shown in Ref. [40], the density of thin antimony layers ρ(Sb) = 5.3 g cm^{-3} when their thickness does not exceed 46 Å. This condition is known to be satisfied for the AMMs under discussion (see Figs 4b, 4d and 4f). At the same time, in thin boron carbide films a density lowering from 2.5 to 2.3 g cm^{-3} is observed even for B_4C layer thickness of ~1000 Å [49]. This is partly due to B_4C layer amorphisation and partly due to modification of its stoichiometry because of the possible presence of oxygen atoms in B_4C magnetron targets. On further lowering of B_4C layer thickness, the material density may also decrease due to its further amorphisation. X-ray diffraction analysis of periodic Sb/B_4C MMs showed that all layers of the MM structure with a period of 42 Å are amorphous, while in an MM with a period of 156 Å there are indications of crystallisation in antimony layers, but not in B_4C layers [40]. Since the true B_4C layer density in the AMMs under study is unknown, curve (*4*) in Fig. 5, which was calculated for $\rho(B_4C)$ = 1.8 g cm^{-3}, serves to illustrate the effect of B_4C layer density lowering on the AMM reflection spectrum. A figure of 1.8 g cm^{-3}3 was borrowed from Ref. [35] and corresponds to a B_4C layer thickness of ~20 Å in La/B_4C structures.

The absolute reflection coefficients of the Sb/B_4C under investigation may be estimated by borrowing from Ref. [39] the ratio between the experimentally measured reflectivities of periodic MMs (at $\lambda_0 \approx 85$ Å) and the reflectivities calculated assuming the tabulated Sb and B_4C densities for bulk materials. The experimental measurements yield approximately twofold lower reflection coefficients than do the calculations. Hence we estimate the AMM reflection coefficients averaged over the optimisation spectral domains: $R \approx 3.0\%$ (AMM for $\Delta\lambda$ = 90–100 Å), $R \approx 3.5\%$ ($\Delta\lambda$ = 95–105 Å), and $R \approx 2.5\%$ ($\Delta\lambda$ = 100–120 Å). In this case, the integral reflectivity $\Im_2 = \int R(\lambda)d\lambda$ in the optimisation domain amounts to 0.3–0.5 Å for all of the AMMs (Table 3). The integral reflectivity of any of the AMMs is several times greater than the integral reflectivity of any of the periodic MMs (made of the same materials) whose principal reflection peaks lie in the same wavelength interval. The highest value $\Im_2 \approx 0.5$ Å corresponds to the long-wavelength AMM for $\Delta\lambda$ = 100–120 Å. In this case, the greater relative width of the working spectral domain is achieved at the cost of a lower average reflectivity in the optimisation domain (Table 3).

Table 3. Measured and calculated optical characteristics of Sb/B_4C AMMs.

Real working spectral domain $\Delta\lambda$/Å	Estimated average reflectivity R (%)	Integral reflectivity/Å	Reciprocal of the relative spectral width $\lambda/\Delta\lambda$
90.5–100.0	3.0	0.3	10
96.5–105,5	3.5	0.3	11
101.5–121.5	2.5	0.5	5.5

Therefore, the Sb/B_4C AMMs synthesised and characterised in our work show promise in the soft X-ray wavelength domain $\lambda < 124$ Å despite the lowering of spectral reflectivities due to the low density of thin antimony layers. The differences of real operating AMM spectral domains from the optimisation ranges do not exceed 1.5 Å (Table 1), so that the AMMs together cover a broad (90.5–121.5 Å) spectral range.

We emphasise once again that one might expect higher reflectivities from Sb/B_4C MMs if attempts met with success to enhance the optical contrast between Sb and B_4C layers. Supposedly this might be made possible by increasing the antimony layer density up to the tabulated value 6.7 g cm^{-3}, for instance by thermal annealing. The first steps in this direction were made by Kopylets et al. [50]. They showed that annealing at temperatures under 250 °C results in only an increase in interlayer roughness (antimony layers remain amorphous in this case), while annealing at higher temperatures induces the transition of antimony to the crystalline state with a density ρ(Sb) = 6.7 g cm^{-3}. However, the crystallisation of antimony layers in an MM is attended with local lens-like antimony swellings due to diffusion, which disrupt the initial multilayer structure [50].

4. Conclusions

We have made three Sb/B_4C aperiodic normal-incidence multilayer mirrors for operation in the spectral domain beyond the L edge of Si ($\lambda < 124$ Å). The Sb/B_4C multilayer structures were theoretically calculated and then deposited by magnetron sputtering on concave substrates without introduction of additional barrier layers. The reflection spectra of the synthesised AMMs were experimentally recorded using a laser-plasma source of SXR radiation. The wavelength ranges 90–100 Å, 95–105 Å, and 100–120 Å were chosen as the

spectral domains for AMM optimisation. The real working spectral domains of the Sb/B_4C AMMs turned out to be shifted to the long-wavelength side and were equal to 90.5–100.0 Å, 96.5–105.5 Å, and 101.5–121.5 Å. The shift does not exceed 1.5 Å.

Numerical calculations of reflection spectra showed that the shifts of the working spectral domains of the AMMs under investigation, as well as the lowering of the absolute values of spectral reflection coefficients, are due to a lowering of the real densities of antimony and boron carbide layers. The lowering of antimony density to $\rho(\mathrm{Sb}) = 5.3$ g cm^{-3} in layers and films of thickness below 46 Å was confirmed in Ref. [40]. The true B_4C layer density in the synthesised AMMs remains unknown.

This work emphasises the importance of knowing exact layer densities in a multilayer structure in the calculation of AMM reflection spectra. Even small density variations may have a strong effect on the optical contrast between the AMM materials, which is bound to affect the spectral reflection coefficient. It was shown that a 20% antimony density variation (from 6.7 to 5.3 g cm^{-3}) in Sb/B_4C structures for a constant B_4C density can lead to more than a twofold lowering of the average AMM reflectivity.

The synthesised aperiodic Sb/B_4C mirrors have exhibited a high temporal stability (the latest measurements of the AMMs were made four years after their fabrication). The integral reflection coefficients of the AMMs under study range from 0.3 to 0.5 Å. Among the aperiodic structures for the 90–124 Å wavelength range synthesised to date, the Sb/B_4C AMMs rank next only to the recently made Mo/Y and Pd/B_4C aperiodic structures [51]. Planned for the future is the use of Sb/B_4C AMMs for recording the line spectra of laboratory laser plasma, including their use as the focusing elements of SXR VLS spectrometers.

Acknowledgements. This work was supported by the Russian Science Foundation (Grant No. 14-12-00506).

References

1. Ragozin E.N., Mednikov K.N., Pertsov A.A., Pirozhkov A.S., Reva A.A., Shestov S.V., Ul'yanov A.S., Vishnyakov E.A. *Proc. SPIE Int. Soc. Opt. Eng*., **7360**, 73600N (2009).
2. Louis E., Yakshin A.E., Tsarfati T., Bijkerk F. *Prog. Surf. Sci*., **86**, 255 (2011).
3. Barysheva M.M., Pestov A.E., Salashchenko N.N., Toropov M.N., Chkhalo N.I. *Phys. Usp*., **55** (7), 681 (2012) [*Usp. Fiz. Nauk*, **182** (7), 727 (2012)].
4. Huang Q., Medvedev V., van de Kruijs R., Yakshin A., Louis E., Bijkerk F. *Appl. Phys. Rev*., **4**, 011104 (2017).
5. Beigman I.L., Levashov V.E., Mednikov K.N., Pirozhkov A.S., Ragozin E.N., Tolstikhina I.Yu. *Quantum Electron*., **37** (11), 1060 (2007) [*Kvantovaya Elektron*., **37** (11), 1060 (2007)].
6. Beigman I.L., Vishnyakov E.A., Luginin M.S., Ragozin E.N., Tolstikhina I.Yu. *Quantum Electron*., **40** (6), 545 (2010) [*Kvantovaya Elektron*., **40** (6), 545 (2010)].
7. Vishnyakov E.A., Kolesnikov A.O., Kuzin A.A., Negrov D.V., Ragozin E.N., Sasorov P.V., Shatokhin A.N. *Quantum Elektron*., **47** (1), 55 (2017) [*Kvantovaya Electron*., **47** (1), 55 (2017)].
8. Vishnyakov E.A., Shcherbakov A.V., Pertsov A.A., Polkovnikov V.N., Pestov A.E., Pariev D.E., Chkhalo N.I. *Proc. SPIE*, **10235**, 102350W (2017).
9. Culhane J.L., Harra L.K., James A.M., et al. *Solar Phys*., **243** (1), 19 (2007).
10. Lemen J.R., Title A.M., Akin D.J., et al. *Solar Phys*., **275** (1-2), 17 (2012).
11. Shestov S., Reva A., Kuzin S. *Astrophys J*., **780** (1), 15 (2014).
12. Vishnyakov E.A., Bogachev S.A., Kirichenko A.S., Reva A.A., Loboda I.P., Malyshev I.V., Ulyanov A.S., Dyatkov S.Yu., Erkhova N.F., Pertsov A.A., Kuzin S.V. *Proc. SPIE*, **10235**, 102350B (2017).
13. Schäfers F., Mertins H.-C., Gaupp A., et al. *Appl. Opt*., **38** (19), 4074 (1999).
14. Louis E., Khorsand A.R., Sobierajski R., et al. *Proc. SPIE*, **7361**, 73610I (2009).
15. Balakireva L.L., Kozhevnikov I.V. *J. X-Ray Sci. Technol*., **6** (2), 150 (1996).
16. Van Loevezijn P., Schlatmann R., Verhoeven J., van Tiggelen B.A., Gullikson E.M. *Appl. Opt*., **35** (19), 3614 (1996).
17. Yakshin A.E., Kozhevnikov I.V., Zoethout E., Louis E., Bijkerk F. *Opt. Express*, **18** (7), 6957 (2010).
18. Kolachevskii N.N., Pirozhkov A.S., Ragozin E.N. *Quantum Elektron*., **30** (5), 428 (2000) [*Kvantovaya Electron*., **30** (5), 428 (2000)].
19. Kozhevnikov I.V., Yakshin A.E., Bijkerk F. *Opt. Express*, **23** (7), 9276 (2015).
20. Parratt L.G. *Phys. Rev*., **95** (4), 359 (1954).
21. Vinogradov A.V., Kozhevnikov I.V. *Trudy FIAN*, **196**, 62 (1989).
22. Kapralov V.G., Korde R., Levashov V.E., Pirozhkov A.S., Ragozin E.N. *Quantum Elektron*., **32** (2), 149 (2002) [*Kvantovaya Electron*., **32** (2), 149 (2002)].
23. Levashov V.E., Mednikov K.N., Pirozhkov A.S., Ragozin E.N. *Radiat. Phys. Chem*., **75** (11), 1819 (2006).
24. Levashov V.E., Mednikov K.N., Pirozhkov A.S., Ragozin E.N. *Quantum Elektron*., **36** (6), 549 (2006) [*Kvantovaya Electron*., **36** (6), 549 (2006)].
25. Kando M., Pirozhkov A.S., Kawase K., et al. *Phys. Rev. Lett*., **103** (23), 235003 (2009).
26. Pirozhkov A.S., Kando M., Esirkepov T.Zh., et al. *Proc. SPIE*, **8140**, 81400A (2011).
27. Beigman I.L., Pirozhkov A.S., Ragozin E.N. *JETP Lett*., **74** (3), 149 (2001) [*Pis'ma Zh. Eksp. Teor. Fiz*., **74** (3), 167 (2001)].
28. Beigman I.L., Pirozhkov A.S., Ragozin E.N. *J. Opt. A: Pure Appl. Opt*., **4**, 433 (2002).
29. Goulielmakis E., Schultze M., Hofstetter M., et al. *Science*, **320**, 1614 (2008).
30. Vishnyakov E.A., Kamenets F.F., Kondratenko V.V., Luginin M.S., Panchenko A.V., Pershin Yu.P., Pirozhkov A.S., Ragozin E.N. *Quantum Elektron*., **42** (2), 143 (2012) [*Kvantovaya Electron*., **42** (2), 143 (2012)].
31. Pirozhkov A.S., Ragozin E.N. *Phys. Usp*., **58** (11), 1095 (2015) [*Usp. Fiz. Nauk*, **185** (11), 1203 (2015)].
32. Artyukov I.A., Zelentsov V.V., Krymskii K.M. Preprint No. 14 (Moscow: P.N. Lebedev Physics Institute RAS, 2000).
33. Skulina K.M., Alford C.S., Bionta R.M., Makowiecki D.M., Gullikson E.M., Soufli R., Kortright J.B., Underwood J.H. *Appl. Opt*., **34** (19), 3727 (1995).
34. Windt D.L., Donguy S., Seely J., Kjornrattanawanich B., Gullikson E.M., Walton C.C., Golub L., DeLuca E. *Proc. SPIE*, **5168**, 1 (2004).
35. Chkhalo N.I., Küstner S., Polkovnikov V.N., Salashchenko N.N., Schäfers F., Starikov S.D. *Appl. Phys. Lett*., **102**, 011602 (2013).
36. Corso A.J., Zuppella P., Windt D.L., Zangrando M., Pelizzo M.G. *Opt. Express*, **20** (7), 8006 (2012).
37. Windt D.L., Gullikson E.M. *Appl. Opt*., **54** (18), 5850 (2015).
38. Vishnyakov E.A., Luginin M.S., Pirozhkov A.S., Ragozin E.N., Startsev S.A. *Quantum Elektron*., **41** (1), 75 (2011) [*Kvantovaya Electron*., **41** (1), 75 (2011)].
39. Vishnyakov E.A., Voronov D.L., Gullikson E.M., Kondratenko V.V., Kopylets I.A., Luginin M.S., Pirozhkov A.S., Ragozin E.N., Shatokhin A.N. *Quantum Elektron*., **43** (7), 666 (2013) [*Kvantovaya Electron*., **43** (7), 666 (2013)].
40. Kopylets I.A., Kondratenko V.V., Zubarev E.N., Voronov D.L., Gullikson E.M., Vishnyakov E.A., Ragozin E.N. *Appl. Surf. Sci*., **307**, 360 (2014).
41. Vishnyakov E.A., Shatokhin A.N., Ragozin E.N. *Quantum Elektron*., **45** (4), 371 (2015) [*Kvantovaya Electron*., **45** (4), 371 (2015)].
42. Vishnyakov E.A., Kolesnikov A.O., Ragozin E.N., Shatokhin A.N. *Quantum Elektron*., **46** (10), 953 (2016) [*Kvantovaya Electron*., **46** (10), 953 (2016)].

43. Ragozin E.N., Belokopytov A.A., Kolesnikov A.O., Muslimov E.R., Shatokhin A.N., Vishnyakov E.A. *Proc. SPIE*, **10235**, 102350L (2017).
44. Vishnyakov E.A., Mednikov K.N., Pertsov A.A., Ragozin E.N., Reva A.A., Ul'yanov A.S., Shestov S.V. *Quantum Elektron*., **39** (5), 474 (2009) [*Kvantovaya Electron*., **39** (5), 474 (2009)].
45. Gullikson E.M., Underwood J.H., Batson P.C. *J. X-Ray Sci. Technol*., **3**, 283 (1992).
46. Kolachevskii N.N., Pirozhkov A.S., Ragozin E.N. *Quantum Elektron*., **28** (9), 821 (1998) [*Kvantovaya Electron*., **25** (9), 843 (1998)].
47. Vishnyakov E.A., Kirichenko A.S., Reva A.A., Rizvanov A.A., Plastinin Ju.A., Kuzin S.V. *Proc. SPIE*, **9905**, 99053G (2016).
48. Henke B.L., Gullikson E.M., Davis J.C. *Atom. Data Nucl. Data Tables*, **54** (2), 181 (1993); Soufli R., Gullikson E.M. *Proc. SPIE*, **3113**, 222 (1997). Files with refined optical scattering factors are available at http://henke.lbl.gov/optical_constants/.
49. Soufli R., Aquila A.L., Salmassi F., Fernández-Perea M., Gullikson E.M. *Appl. Opt*., **47** (25), 4633 (2008).
50. Kopylets I.A., Zubarev E.M., Kondratenko V.V., Sevrukova V.A. *Metallofiz. Noveishie Tekhnol*., **38** (7), 911 (2016).
51. Windt D.L., Gullikson E.M. *Appl. Opt*., **54** (18), 5850 (2015).